

Cryogenic amplifier with low input-referred voltage noise calibrated by shot noise measurement

Wuhao Yang(杨伍昊), Jian Wei(危健)
Citation: Chin. Phys. B . 2018, 27(6): 060702. **doi:** 10.1088/1674-1056/27/6/060702

Journal homepage: http://cpb.iphy.ac.cn; http://iopscience.iop.org/cpb

What follows is a list of articles you may be interested in

4.3 THz quantum-well photodetectors with high detection sensitivity

Zhenzhen Zhang(张真真), Zhanglong Fu(符张龙), Xuguang Guo(郭旭光), Juncheng Cao(曹俊诚)
Chin. Phys. B . 2018, 27(3): 030701. **doi:** 10.1088/1674-1056/27/3/030701

Spin-valley-dependent transport and giant tunneling magnetoresistance in silicene with periodic electromagnetic modulations

Yi-Man Liu(刘一曼), Huai-Hua Shao(邵怀华), Guang-Hui Zhou(周光辉), Hong-Guang Piao(朴红光), Li-Qing Pan(潘礼庆), Min Liu(刘敏)
Chin. Phys. B . 2017, 26(12): 127303. **doi:** 10.1088/1674-1056/26/12/127303

Application of real space Kerker method in simulating gate-all-around nanowire transistors with realistic discrete dopants

Chang-Sheng Li(李长生), Lei Ma(马磊), Jie-Rong Guo(郭杰荣)
Chin. Phys. B . 2017, 26(9): 097301. **doi:** 10.1088/1674-1056/26/9/097301

Quantum transport through a Z-shaped silicene nanoribbon

A Ahmadi Fouladi
Chin. Phys. B . 2017, 26(4): 047304. **doi:** 10.1088/1674-1056/26/4/047304

Crystal structure and thermochemical properties of phase change materials bis(1-octylammonium) tetrachlorochromate

Lu Dong-Fei, Di You-Ying, He Dong-Hua
Chin. Phys. B . 2012, 21(8): 080702. **doi:** 10.1088/1674-1056/21/8/080702

Cryogenic amplifier with low input-referred voltage noise calibrated by shot noise measurement*

Wuhao Yang(杨伍昊)† and Jian Wei(危健)

International Center for Quantum Materials, School of Physics, Peking University, Beijing 100871, *China*

(Received 2 February 2018; revised manuscript received 11 March 2018; published online 10 May 2018)

A low-noise cryogenic amplifier for the bandwidth from 100 kHz to 2 MHz with commercially available components is presented. The amplifier is mounted on the cold finger of our home-made liquid helium dipstick. The input impedance of the amplifier is 2 kΩ. The input-referred voltage noise of the amplifier at approximately 2 MHz is around 1 $\mathrm{nV}/\sqrt{\mathrm{Hz}}$. We demonstrate the performance of the amplifier by measuring shot noise on the Al/AlO_x/Al tunneling junction with resistance about 17 kΩ at liquid helium temperature.

Keywords: cryogenic amplifier, shot noise, shadow evaporation, tunneling junction

PACS: 07.20.Mc, 67.30.hr, 73.23.–b **DOI:** 10.1088/1674-1056/27/6/060702

1. Introduction

Shot noise is nonequilibrium current fluctuations due to the discreteness of charge carriers. It is an important tool for studying correlations induced in mesoscopic transport by different types of interactions. There have been several reports that successfully observed the suppression of the shot noise below the Poissonian limit in a wide range of devices, such as quantum point contacts,[1–4] diffusive wires,[5,6] and quantum dots,[7] which are in agreement with the theoretical prediction.[5,8,9] Recently, some theoretical literatures focused on the Fano factor, the ratio of the actual shot noise and the Poisson noise in Dirac materials. Their numerical calculations have shown that the Fano factor contains important additional information that is not contained in the conductivity.[10,11] Therefore, shot noise measurement can be a useful tool to study the Dirac materials.[12–15] Usually, shot noise measurement is required to be conducted at low temperature and high frequency (over MHz) because of the coexistence of the Johnson–Nyquist noise (thermal noise) and the Flicker noise ($1/f$ noise). Johnson–Nyquist noise can be suppressed by decreasing the temperature of the samples. Flicker noise can be suppressed by increasing the bandwidth. In order to measure the shot noise with high accuracy, a technique that combines an inductor–capacitor (LC) resonant circuit or square law detector with a cryogenic amplifier based on the high electron mobility transistor (HEMT) has been widely used.[16–19] Although this technique has been applied to various mesoscopic devices, observing the overall features of the power spectrum density in a wide frequency range is still challenging because both the LC resonant circuit and the square law detector can only be used for a narrow bandwidth to the amplifier. Moreover, we are interested in measuring the noise of the sample with resistance about 10 kΩ much larger than 50 Ω, because it is in the order of the magnitude of mesoscopic device resistance ($h/2e^2 \sim 13$ kΩ). Therefore, we need a low temperature transimpedance setup to get the power spectrum density in a higher frequency range to suppress the flicker noise.

In this work, we build a low-noise cryogenic amplifier for the bandwidth from 100 kHz to 2 MHz with readily available components. The amplifier has been designed to measure the power spectra density of the shot noise. The amplifier is thermally anchored to the cold finger of our home-made liquid Helium dip stick. The gain and the noise temperature of our amplifier are calibrated using Johnson–Nyquist noise and shot noise of an Al/AlO_x/Al tunneling junction.

The layout of this article is as follows. In Section 2, we present the design of our amplifier and describe the operation. In Section 3, we present the system performance, and the measurement system and the fabrication of the device are presented. In Section 4, the calibration of the gain and the noise temperature of the amplifier are discussed.

2. Design of the amplifier

2.1. Overview of circuit

Figure 1(a) shows the schematic diagram of our amplifier and the layout of the amplifier. The amplification line consists of two parts interconnected by two coaxial cables (50-Ω impedance), as shown in the circuit schematic diagram in Fig. 1(a). The cryogenic part is thermally anchored to the cold finger of our home-made liquid helium dip stick. The room temperature part consists of two variable resistors and a 12-V lead-acid battery, which are in an aluminum box for shielding.

*Project supported by the National Natural Science Foundation of China (Grant No. 11474008), the National Key Research and Development Program of China (Grant No. 2016YFA0300904), and the National Basic Research Program of China (Grant No. 2011CBA00106).

†Corresponding author. E-mail: yangwuhao@pku.edu.cn

© 2018 Chinese Physical Society and IOP Publishing Ltd

The cryogenic part is made on a one-side surface copper coating printed-circuit board (FR-4 glass epoxy) with commercial discrete components and it is placed in a copper shielding box (the outer size is 20 mm×31 mm) as shown in Fig. 1(c). Four SMB connectors interconnect the amplifier and the outside of the copper shielding box. Figure 1(b) shows a schematic of the printed-circuit board. The size of the printed-circuit board is 10 mm×20 mm and the metal (yellow regions) is patterned by chemical etching. The HEMT (Agilent ATF-34143) is the only active component in the circuit. All the cryogenic resistors are Susumu 0805-size surface mount thin metal film resistors from Mouser electronics. The cryogenic capacitors are 0805-size surface mount (Murata C0G GRM2165 multilayer ceramic capacitor) except $C_{\rm in}$, which is a leaded ceramic capacitor that protects the HEMT from breakdown. Two sets of 10-Ω resistors and 100-nF capacitors are used for the two source leads of ATF-34143 to avoid the interference of the ground. These passive components with small temperature coefficients play a role in stabilizing the amplifier.

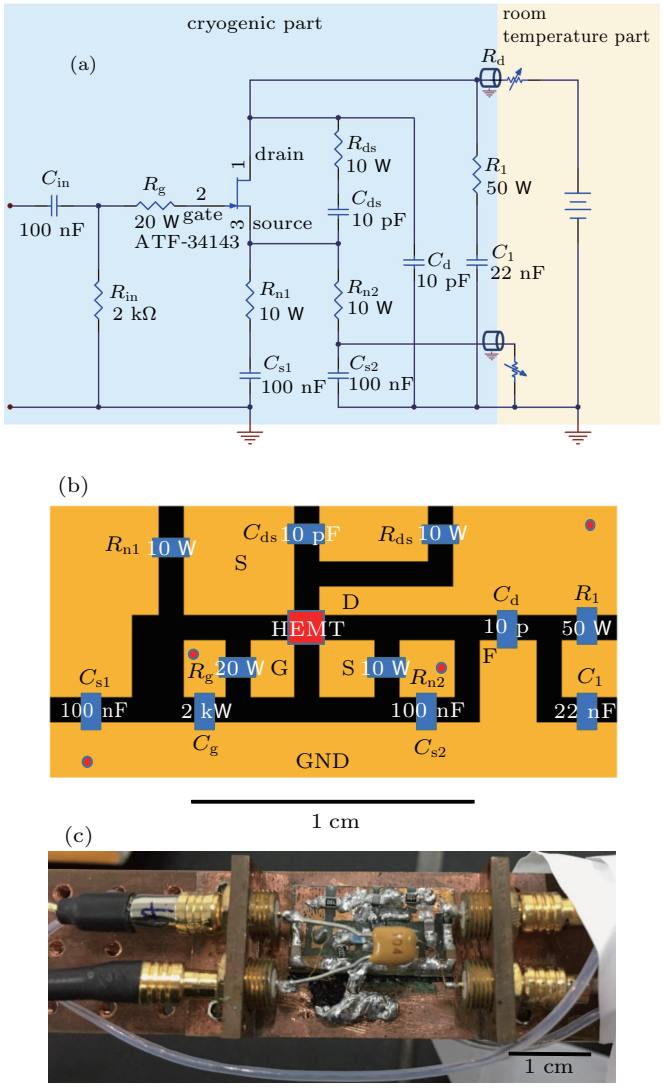


Fig. 1. (color online) (a) Circuit schematic diagram of our amplifier. (b) Layout of the CRYOAMP circuit board. Metal (yellow regions) is patterned by etching one-side surface copper coating FR-4 glass epoxy, whose size is 1 cm×2 cm. Four red points show the solder points on the printed-circuit board, which connect the inner pin of the connector. (c) Photograph of a CRYOAMP circuit board.

2.2. Operation

The HEMT must be biased in saturation to provide voltage (transconductance) gain in the low (high) frequency range. Figure 2 shows the DC characteristics of the cryogenic part of the amplifier at (a) room temperature and (b) liquid helium temperature. $V_{{\rm d}-10R}$ is the voltage between the drain of HEMT and the 10-Ω resistor $R_{\rm n2}$, and $V_{\rm g}$ is the voltage between the gate and ground. According to previous implementations of the similar circuits, the DC characteristics of the HEMT varies a little.[16,17] However, the large $V_{{\rm d}-10R}$ can cause a shift in the dc characteristics at the low temperature. If we bias the $I_{\rm ds}$ between 0.2 mA ∼ 0.8 mA, we can estimate that the transconductance of the HEMT is about 5 mS ∼ 20 mS, which is slightly smaller at room temperature (RT) than at liquid helium temperature, as shown in Fig. 2. The room temperature part in Fig. 1(a) that consists of a 12-V lead-acid battery and two variable resistors determine the HEMT operating point. Thus we choose proper $R_{\rm s}$ (880 Ω at room temperature and 500 Ω at liquid helium temperature) and proper $R_{\rm d}$ to bias the HEMT to the proper quiescent operating point ($V_{{\rm d}-10R}$ ∼ 0.2 V, $I_{\rm ds}$ ∼ 0.6 mA). The gain of the HEMT amplifier is 0.5 and flat in the frequency range of interest (500 kHz to 8 MHz) at liquid helium temperature, which is measured by a function generator and 50 MHz digitizer with an input impedance of 50 Ω. The result is shown in Fig. 3. The DC equivalent effective circuit is shown in Fig. 4(a) and the AC equivalent effective circuit is shown in Fig. 4(b). The output signal of the HEMT amplifier is amplified by a 50-Ω amplifier with a gain of 60 dB at room temperature.

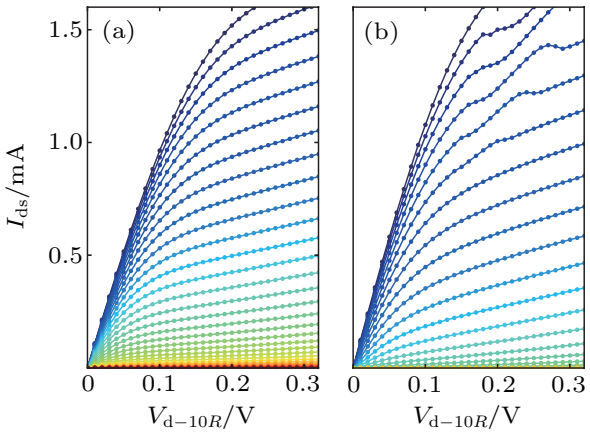


Fig. 2. (color online) Typical DC characteristics of the cryogenic part of the amplifier at (a) room temperature and (b) liquid helium temperature. (a) $V_{\rm g}$ varies from −0.40 V (top) to −0.75 V (bottom) in 0.01-V steps. (b) $V_{\rm g}$ varies from −0.25 V (top) to −0.49 V (bottom) in 0.01-V steps.

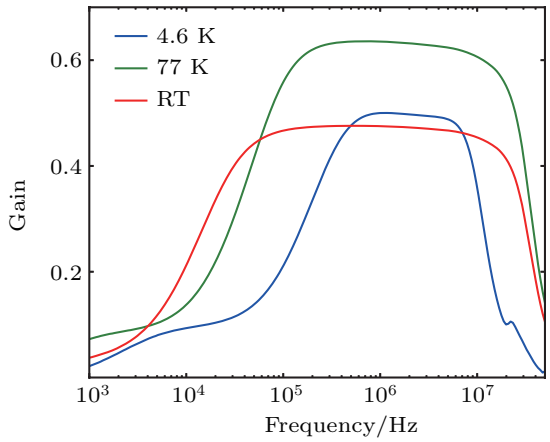


Fig. 3. (color online) The frequency dependence of the voltage gain of the cryogenic amplifier into a 50-Ω load, measured for the quiescent operating points at room temperature (red line), liquid nitrogen temperature (green line), and liquid helium temperature (blue line).

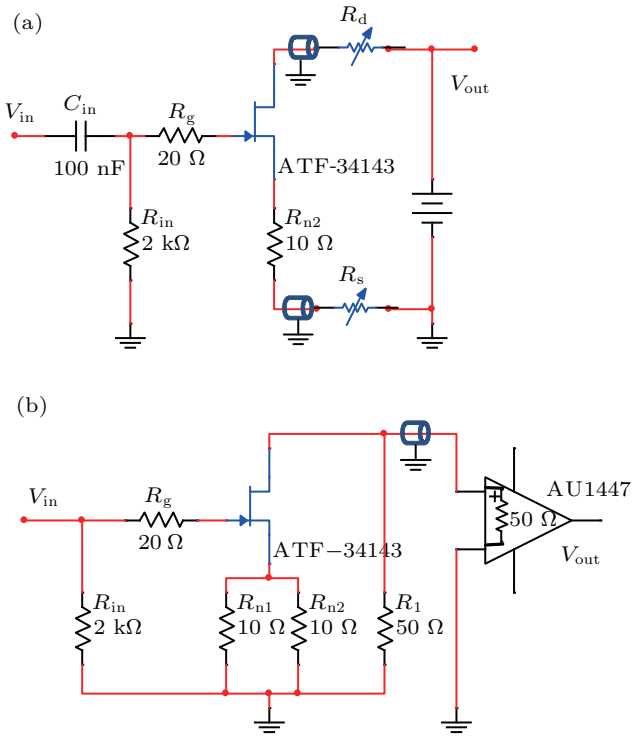


Fig. 4. (color online) Equivalent effective circuits: (a) DC bias circuits and (b) AC signal circuits.

3. System performance

3.1. Setup

Our noise measurement system is installed on our home-made liquid helium dip stick. The cryogenic part in Fig. 1(a) is thermally anchored to the cold finger. Figure 5 shows the schematic of our measurement setup. We use a voltage source and a 1-MΩ ballast resistor in series to supply the current. For the transport measurement, we use a digital voltage meter (DVM) to measure the voltage. Since the capacitance of the transport line can shunt the noise signal of the sample for the noise measurement, we use two cryogenic resistors (15-kΩ Susumu 0805-size thin metal film resistor) with resistance similar to that of the sample in series, and fix them on the sample holder close to the sample, as shown in the left part of Fig. 5. For the noise measurement, the noise signal of the sample is amplified by our cryogenic amplifier at liquid helium temperature and the 50-Ω amplifier (MITEQ AU-1447) with a gain of 60 dB and a noise temperature of 92.3 K in the range of 0.01 MHz–200 MHz, then the time domain signal is taken by a data acquisition card (ADLINK PCI-9846H/512), as shown in the right part of Fig. 5. Then we obtain the spectrum and power spectrum density by performing the fast fourier transformation (FFT) for the data. Impedance matching to avoid signal attenuation is taken into account as the input impedance and the output impedance of the Au-1447 is 50 Ω. To block the dc current, we use a DC block (Mini-circuits BLK-89-S+ with the range of 0.1 MHz–8000 MHz) between the cryogenic amplifier and the Au-1447 amplifier. To avoid the frequency aliasing, we use an anti-aliasing filter (Mini-circuits BLP-10.7+ low pass filter) between the data acquisition card and the Au-1447 amplifier. According to the measured frequency dependence of the gain of the HEMT amplifier in Fig. 3, we estimate the frequency dependence of the total gain of the system with the same method. Although it is not constant in the frequency range of interest (500 kHz to 8 MHz), it is flat enough to average for the frequency bin we select, 2 MHz to 2.1 MHz, the gain is about 590. The total gain is also calibrated by the thermal noise measurement for 10 Ω, 1 kΩ, 5 kΩ, 10 kΩ thin film resistors at room temperature and liquid helium temperature.

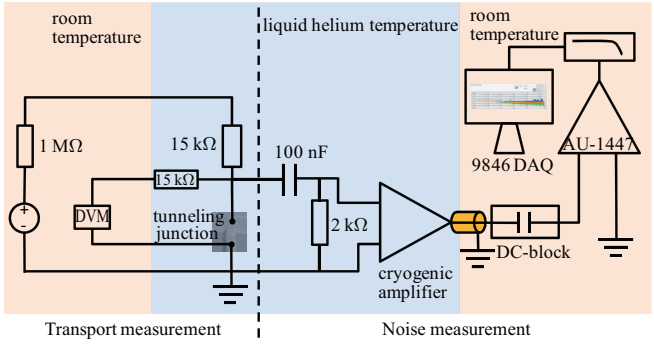


Fig. 5. (color online) Schematic diagram of the measurement setup with the transport measurement part and the noise measurement part. The transport measurement includes four lines (twisted pair cable), while the noise measurement includes four coaxial cables. Only one coaxial cable which is as output line is shown in this figure for simplicity.

3.2. Device

We demonstrate the performance of our noise measurement system by measuring shot noise on a tunneling junction. The tunneling junction is fabricated on one-side polished silicon covered by a 300-nm oxidized layer. In order to create a very clean interface of the oxidation layer and a well-controlled tunneling junction, we use the shadow evaporation method, in which the top layer aluminum film was deposited on the bottom layer aluminum film at different an-

gles through a shadow mask after *in-situ* oxidation of the bottom layer aluminum without breaking the vacuum.[20–23] The shadow mask is defined by PMGI/PMMA bilayer electron-beam lithography on the Ti/Au pad for wire bonding, which is fabricated by standard bilayer UV lithography and lift-off techniques, as shown in Figs. 6(a) and 6(b). To test our amplifier, we choose the resistance of the tunneling junction to be ~ 10 kΩ, because large resistance of the tunneling junction limits the bandwidth of the observed spectrum, while smaller sample resistance makes it difficult for the amplification to measure the current noise. Thus we choose the deposition and oxidation parameter carefully. To maintain directional deposition and less coating on side walls, aluminum films are deposited at ~ 1 Å/s by the thermal evaporator system with base pressure below 1×10^{-6} Torr (1 Torr = 1.33322×10^2 Pa). To ensure the ohmic contact, we deposit 28-nm first layer aluminum film along the direction normal to the substrate with 25-nm Ti/Au pad, and 50-nm second layer aluminum film at a 30° angle to the substrate and parallel slit in Fig. 6(a). To ensure the uniform oxidation and avoid the pin holes in the oxidation layer, the first layer aluminum is oxidized in 1.92-Torr argon mixed with 0.338-Torr oxygen for 3 min. The area of the tunneling junction is controlled by the geometry of the shadow mask and the deposition angles of the second layer aluminum. The scanning electron microscopy (SEM) image of Al/AlO$_x$/Al tunneling junction is shown in Fig. 6(c).

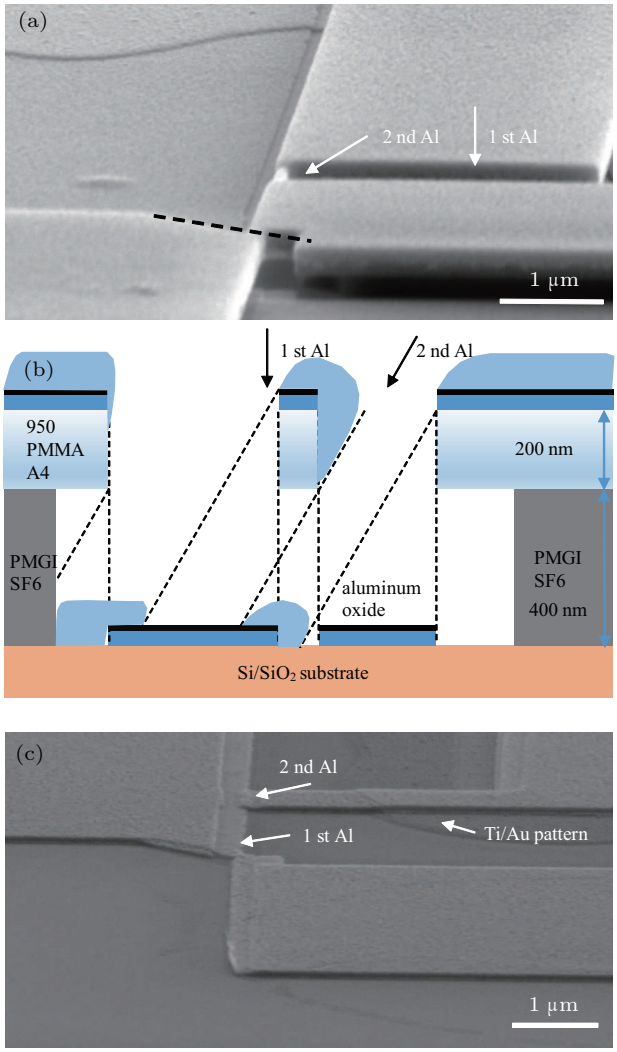


Fig. 6. (color online) Fabrication of Al/AlO$_x$/Al tunneling junction. (a) SEM image of the shadow mask taken after the deposition of Aluminum films and before lift-off. The bilayer shadow mask consists of a top 200-nm thick polymethyl methacrylate (950 A4 PMMA) layer, used as a high-resolution electron resist, and a bottom 400-nm thick layer of polymer polydimethylglutarimide (PMGI SF6). A deep undercut in the bottom layer allows for overlapping of the films deposited at different incident angles. (b) Cross-section along the dashed line in panel (a). The first layer Al is deposited along the direction normal to the plane of the substrate, the second layer Al is deposited at a 30° incidence angle and parallel slit in panel (a). (c) SEM image of Al/AlO$_x$/Al tunneling junction with dimensions 180 nm×1000 nm×70 nm. The 1st layer Al and the 2nd layer Al overlap on the different Ti/Au pattern leads, which we fabricated by UV lithography.

3.3. Measurement

Differential resistance measurement is performed with conventional lock-in techniques. The part of the circuit for transport measurement is shown in Fig. 5. Figure 7 shows the differential resistance of the tunneling junction as a function of temperature during warming up, which is typical for this kind of junction. The upper inset shows the SEM images of the device we measured. The lower inset shows the differential resistance as a function of the current bias at 4.6 K.

We measured the total noise spectral density at 4.6 K and normalized them using the total gain of our noise measurement setup at 2 MHz as an equivalent input referred voltage noise, which is shown in Fig. 8(a). A characteristic 1/f contribution is present up to 100 kHz. The drop of the noise power from 100 Hz to 1000 Hz is caused by the DC block in Fig. 5. The spectrum from 100 kHz to 2 MHz is dominated by the thermal noise of the system and the shot noise of the junction. The spectrum also reveals the change of the voltage gain of the HEMT.[16] The extra noise over 2 MHz may be caused by the shielding problem or resonance effect with the filter. We pick the spectrum in the frequency bin, 2 MHz to 2.1 MHz, that is flat enough to average, as shown in the inset in Fig. 8(a). The bias dependence of the voltage noise power that is related to the current noise power S_I by $S_\mathrm{V} = S_\mathrm{I} R_\mathrm{d}^2$ is plotted in Fig. 8(b). R_d is the differential resistance of the tunneling junction, as shown in the inset in Fig. 7. The current noise power S_I is fitted using the following equation by considering the contribution of the background noise (including the thermal noise of the system) of the system.[24]

$$S_\mathrm{I} = 2F\left[\frac{eV}{R_\mathrm{d}}\coth\left(\frac{eV}{2k_\mathrm{B}T}\right) - \frac{2k_\mathrm{B}T}{R_\mathrm{d}}\right] + \frac{4k_\mathrm{B}T}{R_\mathrm{d}}, \qquad (1)$$

where F is the Fano factor, T is device temperature, which is measured by the Cernox-1070 thermometry mounted on the cold finger, and k_B is the Boltzmann constant. The Fano factor F and the background noise BG (include the thermal noise

of the system) of the system are the fitting parameters. Using Eq. (1), we can fit the Fano factor F of the Al/AlO$_x$/Al tunneling junction and the background noise BG. The results are shown in Fig. 8(b), F is 0.998, and BG is 1.04 nV/$\sqrt{\text{Hz}}$. We also select other frequency bins to average and conduct similar fitting using the total gain in Subsection 3.1 (details are given in Appendix A). The results are consistent.

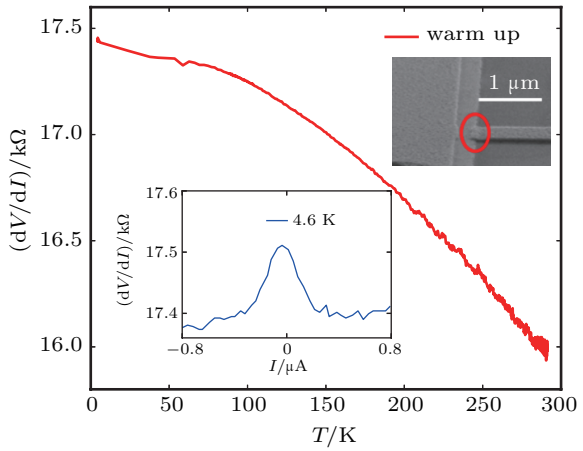


Fig. 7. (color online) Differential resistance as a function of temperature. Inset: Upper right shows the SEM image of the Al/AlO$_x$/Al tunneling junction (red circle). Lower left shows the differential resistance as a function of the current bias at 4.6 K.

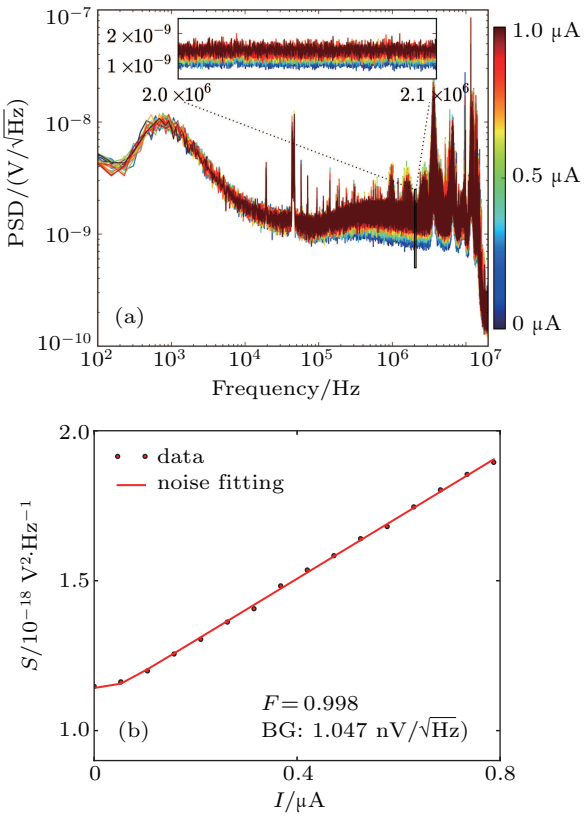


Fig. 8. (color online) (a) Voltage noise spectrum for different current bias of the Al/AlO$_x$/Al tunneling junction at 4.6 K, which is measured by our cryogenic amplifier with Au-1447 amplifier. Current bias varies from 0 μA to 1 μA in 0.05-μA steps. Inset: Zoom-in of the voltage noise spectrum in the frequency bin we pick with linear axis, 2.0 MHz to 2.1 MHz (black rectangle). (b) The bias dependence of the voltage noise power of the Al/AlO$_x$/Al tunneling junction at 4.6 K measured by our cryogenic amplifier with Au-1447 amplifier.

For comparison, we have conducted a similar measurement using a different noise measurement setup, which consists of our home-made room temperature pre-amplifier (the input impedance of the amplifier is 100 MΩ) and data acquisition card (National Instruments PCI-4474).[25,26] The voltage noise spectrum that is normalized by the gain of the home-made room temperature pre-amplifier at 1 kHz for different current bias is shown in Fig. 9(a). The voltage noise power differs by an order of magnitude from Fig. 8(a) because of the different input impedance of the amplifier. The inset shows the spectrum in the frequency bin we pick, 1 kHz to 1.5 kHz, that is flat enough to average. The fitting results are shown in Fig. 9(b). The Fano factor F is 0.964 that is consistent with the results in Fig. 8(b), while the background noise BG is 3.094 nV/$\sqrt{\text{Hz}}$, which is larger than that in Fig. 8(b).

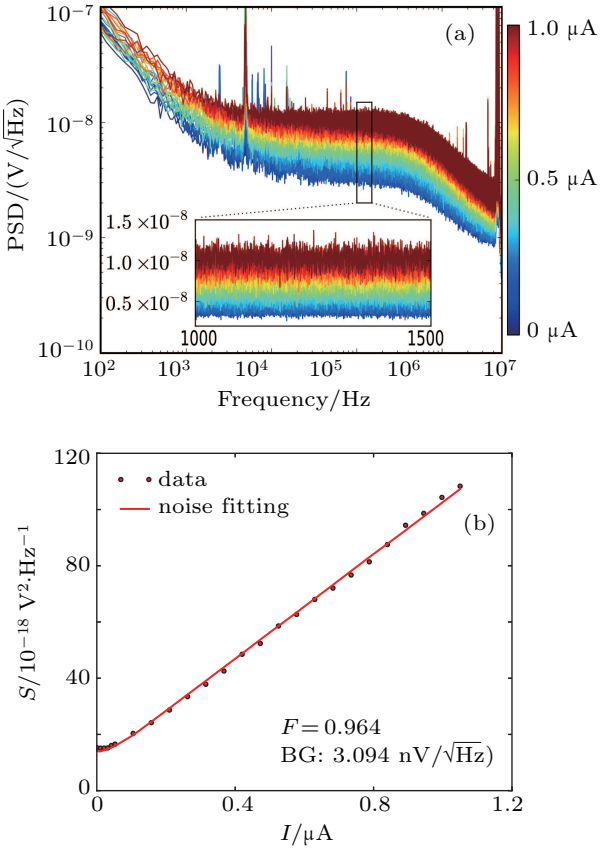


Fig. 9. (color online) (a) Voltage noise spectrum for different current bias of the Al/AlO$_x$/Al tunneling junction at 4.6 K, which is measured by our room temperature pre-amplifier. Current bias varies from 0 μA to 1 μA in 0.05-μA steps. Inset: Zoom-in of the voltage noise spectrum in the frequency bin we pick with linear axis, 1.0 kHz to 1.5 kHz (black rectangle). (b) The bias dependence of the voltage noise power of the Al/AlO$_x$/Al tunneling junction at 4.6 K measured by our room temperature pre-amplifier.

4. Conclusion and discussion

In conclusion, we design a HEMT-based cryogenic amplifier with discrete components on our home-made liquid helium dip stick and build a noise measurement system with it. We estimate the frequency dependence of the total gain

of the system with transimpedance method. The frequency-dependent gain is also confirmed by the shot noise measurement, which is flat enough to average for the frequency bin we selected, 2 MHz to 2.1 MHz, the gain is about 590. Using a data acquisition card and performing the fast Fourier transform (FFT) for the data, we obtain the spectrum density for the bandwidth from 1 Hz to 20 MHz. We fabricate an Al/AlO_x/Al tunneling junction with resistance about 17 kΩ and use its noise property to demonstrate the performance of the system. The effective bandwidth of the system is 100 kHz to 3 MHz, and the equivalent input referred voltage noise lower than 1.04 nV/$\sqrt{\text{Hz}}$. We believe that such a high-performance cryogenic amplifier setup will be useful to explore mesoscopic nonequilibrium statistical physics.[27]

Appendix A: Estimation of the total gain of the system

As described in Subsection 3.1, the total gain of the system is not constant in the frequency range of interest. Thus we measure the total gain at some typical frequency bin and verify that by the fitting of the Fano factor of the Al/AlO_x/Al tunneling junction. The total gain is 620 in the frequency bin from 500 kHz to 510 kHz, using it we fit the Fano factor F is 0.976 and the background noise BG is 1.148 nV/$\sqrt{\text{Hz}}$, as shown in Fig. 10(a). Similarly, the total gain is 630 in the frequency bin from 800 kHz to 810 kHz and 620 in the frequency bin from 1.2 MHz to 1.21 MHz. The fitting results are consistent, as shown in Figs. S1(b) and S1(c).

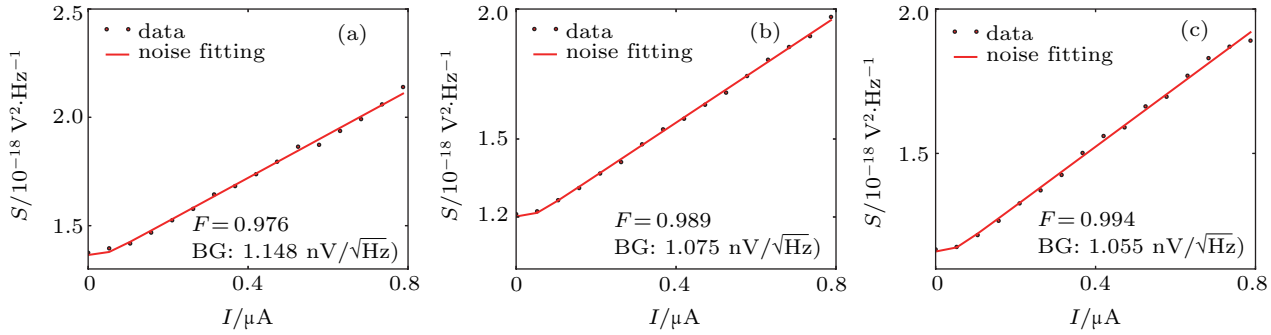


Fig. S1. (color online) The bias dependence of the voltage noise power of the Al/AlO_x/Al tunneling junction at 4.6 K measured by our cryogenic amplifier with Au-1447 amplifier using the spectrum of a different frequency bin. (a) The total gain is 620 in the frequency bin from 500 kHz to 510 kHz. (b) The total gain is 630 in the frequency bin from 800 kHz to 810 kHz. (c) The total gain is 620 in the frequency bin from 1.2 MHz to 1.21 MHz.

Acknowledgment

We thank Zhou Huibin, Niu Jiasen, Yang Fang and other students in our laboratory for help during the experiment, and thank professor Lin Xi for valuable discussion. We acknowledge support by Nanofab ICQM, Peking University and its manager Luo Qiang, for fabrication of tunnel junction devices.

References

[1] Reznikov M, Heiblum M, Shtrikman H and Mahalu D 1995 *Phys. Rev. Lett.* **75** 3340
[2] Kumar A, Saminadayar L, Glattli D C, Jin Y and Etienne B 1996 *Phys. Rev. Lett.* **76** 2778
[3] Liu R C Odom B, Yamamoto Y and Tarucha S 1998 *Nature* **391** 263
[4] Wagner T, Strasberg P, Bayer J C, Rugeramigabo E P, Brandes T and Haug R J 2017 *Nat. Nanotechnol.* **12** 218
[5] Steinbach A H, Martinis J M and Devoret M H 1996 *Phys. Rev. Lett.* **76** 3806
[6] Henny M, Oberholzer S, Strunk C and Schönenberger C 1999 *Phys. Rev. B* **59** 2871
[7] Oberholzer S, Sukhorukov E V, Strunk C and Schönenberger C 2001 *Phys. Rev. Lett.* **86** 2114
[8] Beenakker C W J and Büttiker M. 1992 *Phys. Rev. B* **46** 1889
[9] Blanter Y M and Sukhorukov E V 2000 *Phys. Rev. Lett.* **84** 1280
[10] Sbierski B and Pohl G and Bergholtz E J and Brouwer P W 2014 *Phys. Rev. Lett.* **113** 026602
[11] Trescher M, Sbierski B and Brouwer P W and Bergholtz E J 2014 *Phys. Rev. B* **91** 115135
[12] Fang Z, Nagaosa N, Takahashi K S, Mathieu R, Ogasawara T, Yamada H, Kawasaki M, Tokura Y and Terakura K 2003 *Science* **302** 92
[13] Murakami S 2007 *New J. Phys.* **9** 356
[14] Liu Z K, Zhou B, Zhang Y, Wang Z J, Weng M H, Prabhakaran D, Mo S K, Shen Z X, Fang Z, Dai X, Hussain Z and Chen Y L 2014 *Science* **343** 864
[15] Liu Z K, Jiang J, Zhou B, Wang Z J, Zhang Y, Weng H M, Prabhakaran D, Mo S K, Peng H, Dudin P, Kim T, Hoesch M, Fang Z, Dai X, Shen Z X, Feng D L, Hussain Z and Chen Y L 2014 *Nat. Mater.* **13** 677
[16] Robinson A M and Talyanskii V I 2004 *Rev. Sci. Instrum.* **75** 3169
[17] DiCarlo L, Zhang Y, McClure D T, Marcus C M, Pfeiffer L N and West K W 2006 *Rev. Sci. Instrum.* **77** 073906
[18] Hashisaka M, Nakamura S, Yamauchi Y, Kasai S, Kobayashi K and Ono T 2008 *Phys. Status Solidi (c)* **5** 182
[19] Hashisaka M, Yamauchi Y, Nakamura S, Kasai S, Kobayashi K and Ono T 2008 *J. Phys.: Conf. Ser.* **109** 012013
[20] Fulton T A and Dolan G J 1987 *Phys. Rev. Lett.* **59** 109
[21] Dolan G J 1977 *Phys. Rev. Lett.* **31** 337
[22] Pop I M. Fournier T, Crozes T, Lecocq F, Matei I, Pannetier B, Buisson O and Guichard W 2012 *J. Vac. Sci. Technol. B* **30** 010607
[23] Wei J, Olaya D, Karasik B S, Pereverzev S V, Sergeev A V and Gershenson M E 2008 *Nat. Nanotechnol.* **3** 496
[24] Blanter Y M, Büttiker M 2000 *Phys. Rep.* **336** 1
[25] Guo H, Tang W, Liu L, Wei J, Li D, Feng J and Han X 2015 *Chin. Phys. B* **24** 078504
[26] Liu L, Niu J, Guo H, Wei J, Li D L, Feng J F, Han X F, Coey J M D and Zhang X G 2016 *Phys. Rev. B* **93** 18
[27] Nakamura S, Yamauchi Y, Masayuki H, Chida K, Kobayashi K, Ono T, Leturcq R, Ensslin K, Saito K, Utsumi Y and Gossard A C 2010 *Phys. Rev. Lett.* **104** 080602